Journal of Power Sources 196 (2011) 7891–7898

Contents lists available at ScienceDirect

Journal of Power Sources

journal homepage: www.elsevier.com/locate/jpowsour

Dye-sensitized solar cells based on anatase TiO_2 hollow spheres/carbon nanotube composite films

Jiaguo Yu*, Jiajie Fan, Bei Cheng

State Key Laboratory of Advanced Technology for Materials Synthesis and Processing, Wuhan University of Technology, Wuhan, 430070, PR China

ARTICLE INFO

Article history:
Received 10 January 2011
Received in revised form 7 April 2011
Accepted 10 May 2011
Available online 19 May 2011

Keywords:
Anatase TiO_2 hollow spheres
Multi-walled carbon nanotubes (CNT)
Composite
Dye-sensitized solar cells (DSSCs)

ABSTRACT

Dye-sensitized solar cells (DSSCs) based on anatase TiO_2 hollow spheres (TiO2HS)/multi-walled carbon nanotubes (CNT) nanocomposite films are prepared by a directly mechanical mixing and doctor blade method. The prepared samples are characterized by scanning electron microscopy, transmission electron microscopy, X-ray diffraction, UV–vis absorption spectroscopy and N_2 adsorption–desorption isotherms. The photoelectric conversion performances of the DSSCs based on TiO2HS/CNT composite film electrodes are also compared with commercial-grade Degussa P25 TiO_2 nanoparticles (P25)/CNT composite solar cells at the same film thickness. The results indicate that the photoelectric conversion efficiencies (η) of the TiO2HS/CNT composite DSSCs are dependent on CNT loading in the electrodes. A small amount of CNT clearly enhances DSSC efficiency, while excessive CNT loading significantly lowers their performance. The former is because CNT enhance the transport of electrons from the films to FTO substrates. The latter is due to high CNT loading shielding the visible light from being adsorbed by dyes.

1. Introduction

Since the first report on low-cost dye-sensitized solar cells (DSSCs) based on TiO_2 nanocrystalline mesoporous particle films was published in 1991 by O'Regan and Gratzel [1], great efforts have been made to improve the performance of the DSSCs [2–4]. Nevertheless, despite their initial success of approximately 11% solar conversion efficiency, continued efforts to improve cell performance have not made greater breakthroughs [5–7]. Typically, DSSCs consist of a nanocrystalline porous TiO_2 film covered by a monolayer of dye molecules, a redox-active liquid electrolyte (iodide/tri-iodide based), and a Pt counter electrode [1]. Among the above three parts, the preparation of porous TiO_2 film is a key factor in the optimization of DSSCs for its enormous influence on the anchor of dye molecules and transfer and separation of charge carriers [8,9]. In the operation of DSSCs, sunlight is first absorbed by the dye molecules anchored to the TiO_2 surface and excites electrons from highest occupied molecular orbitals (HOMO) to lowest unoccupied molecular orbitals (LUMO) of the dye, and the excited-state electrons are quickly injected into the conduction band of TiO_2. These electrons diffuse through the TiO_2 particle network to the collecting transparent conducting oxide (TCO) substrate. The oxidized dye molecules are regenerated by the reducing species in the electrolyte solution, predominately I^- ions, and then the resulting tri-iodide ions can accept electrons from the platinized TCO counter electrode to fulfill a complete current cycle in DSSCs [3,4]. The rapid electron transport and transfer in the porous TiO_2 films are pivotal in reducing photo-generated electron-hole recombination and in improving the photoelectric conversion efficiencies (η) of the DSSCs [3,9]. Fabrication of porous films using one-dimensional (1D) nano-structures has proven to be a good way to improve electron transport [10,11]. In addition to the effect on electron transport, 1D nano-structure also enhances the light harvesting by scattering of light. However, in most conventional DSSCs, TiO_2 nanoparicles with sizes of 10–20 nm are used. The particle sizes are much smaller than the wavelength of visible light. Therefore, the film is transparent due to little scattering of light.

In recent years, carbon nanotubes have attracted more and more attention due to their special electric structure, large specific surface area, hollow and layered structures, extraordinary mechanical and chemical stability properties and their widely potential applications [12]. Especially, carbon nanotubes not only have a large electrons-storage capacity, but also show electronic conductivity similar to that of metals [13]. Taking account of their 1D nano-structures and good electrical conductivity, it is reasonable to conclude that CNT/TiO_2 composites are beneficial to transport the electrons within TiO_2 films and enhance their photocatalytic and photoelectric conversion efficiencies [14]. Many experimental results have confirmed this point. For example, Yu et al. reported that CNT/TiO_2 composites obtained by ultrasonic irradiation showed the enhanced photocatalytic activity toward decomposing gas acetone in air as well as azo dyes in water [15].

* Corresponding author. Tel.: +86 27 87871029; fax: +86 27 87879468.
E-mail address: jiaguoyu@yahoo.com (J. Yu).

0378-7753/$ – see front matter © 2011 Elsevier B.V. All rights reserved.
doi:10.1016/j.jpowsour.2011.05.014

Table 1
The physicochemical properties of P25, acid-treated CNT, and TiO2HS/CNT composite powders scraped from the composite film electrodes.

Samples	CNT (wt%)	S_{BET} ($m^2\ g^{-1}$)	PV ($cm^3\ g^{-1}$)	APS (nm)	Porosity (%)	ACS (nm)	RC
CT-0	0	82	0.27	15.0	51.3	15.7 (A)	1
CT-0.05	0.05	83	0.29	14.8	53.1	15.4 (A)	0.96
CT-0.1	0.1	85	0.30	14.4	54.0	15.1 (A)	0.94
CT-0.2	0.2	88	0.32	14.1	55.6	14.8 (A)	0.91
CT-0.5	0.5	90	0.33	13.7	56.3	14.4 (A)	0.88
CT-1.0	1	93	0.36	13.3	58.4	13.9 (A)	0.79
CNT	100	244	1.19	17.8	67.6	–	–
P25	–	45	0.15	13.6	36.9	24.5 (A)	–

A: anatase; PV: pore volume; APS: average pore size; ACS: average crystallite size; RC: Relative crystallinity.

Muduli et al. demonstrated the enhanced conversion efficiency in dye-sensitized solar cells based on the hydrothermally synthesized TiO_2–MWCNT nanocomposites [16]. Lee et al. reported DSSCs based on nanocomposites of preprocessed multi-walled CNT (MWCNT) with carboxylic acid groups and TiO_2 nanoparticles (NPs) synthesized via a sol–gel process, showing a conversion efficiency of 4.97% [17]. Yen et al. synthesized MWCNT–TiO_2 nanocomposites by a modified acid-catalyzed sol–gel method and examined their application in DSSCs, and emphasized the importance of optimum MWCNT loading to realize an efficiency of 4.62% [18]. Kim et al. further obtained a DSSC efficiency of 5.02% using MWCNT–TiO_2 nanocomposites, which exhibit enhancement by ~50% over the case without MWCNT [19]. More recently, Sawatsuk et al. have shown the improvement in the efficiency of DSSC by almost 60% by a simple mixing process [20].

TiO_2 is a very important multifunctional material because of its peculiar and fascinating physicochemical properties and a wide variety of potential application in diverse fields including solar energy conversion, environmental purification, and water treatment [21–24]. In particular, TiO_2 hollow structured materials have received extensive attention owing to their low density, high specific surface areas, and good photocatalytic activity [25–28]. Generally, the morphology, porous structure and crystallite size of TiO_2 play important roles in the photoelectric properties of DSSCs [29]. Based on the advances in nanosized TiO_2, this material has been regarded as a superior candidate for the fabrication of porous photoanode film [30,31]. However, to the best of our knowledge, there are few reports focusing on the fabrication of anatase TiO_2 hollow spheres (TiO2HS)/CNT composite film electrodes and their application in DSSCs. In this work, TiO2HS/CNT composite films are for the first time applied to prepare the photoanodes of DSSCs and their performance are investigated and discussed by comparing with pure TiO_2 hollow sphere and P25 DSSCs.

2. Experimental

2.1. Materials preparation

All reagents were analytical grade (purchased from Shanghai Chemical Reagent Factory of China) and used without further purification. CNT were provided by Beijing Key Lab of Green Chemical Engineering, Tsinghua University, Beijing, P.R. China. Generation of functional groups (hydroxyl groups (–OH), carboxyl groups (–COOH) and carbonyl groups (>C=O), etc.) on the surface of CNT can be realized by chemical oxidation treatments [32–34]. In a typical process, the CNT (300 mg) was oxidized in 40 mL of 1:3 (v:v) concentrated nitric acid–sulfuric acids mixed solution under ultrasonication irradiation at 60 °C for 10 h [33]. Then, the CNT were filtered, washed with distilled water several times until the pH value was ca. 6. The product was subsequently dried in a vacuum oven at 40 °C for 12 h.

Anatase TiO_2 hollow spheres were prepared by the template-free chemically induced self-transformation (CIST) method [28]. In a typical synthesis, $Ti(SO_4)_2$ (0.015 mol) was added to 150 mL of distilled water under vigorous stirring for 30 min. Then, 0.015 mol NH_4F and 0.03 mol urea were added to the above mixed solution. After stirring for another 30 min, the mixed solution was transferred to a 200 mL Teflon-lined stainless steel autoclave. The autoclave was kept at 180 °C for 12 h and then air cooled to room temperature. After reaction, the pH value of the solution was ca. 8–9. The white precipitate was collected and washed with distilled water and anhydrous alcohol three times. The final product was dried in a vacuum oven at 80 °C for 12 h.

2.2. Fabrication of TiO2HS/CNT nanocomposite DSSCs

To prepare TiO2HS/CNT composite film electrodes [29], 0–0.015 g (0–1.0 wt%) of acid-treated CNT were dispersed in a mixed solution of 6.5 mL dry alcohol, 2.0 mL distilled water, 0.50 mL acetylacetone and 1.12 mL Triton X-100, then mixed with 1.5 g of TiO2HS in an agate mortar and grinding by hand for 40 min. The TiO2HS/CNT composite films were prepared by the doctor blade method. The F-doped SnO_2-coated glass (FTO glass) (Nippon sheet glass, 14-20 Ω/square, Nippon Co., Tokyo, Japan) was used as substrates. For comparison, the electrodes were also prepared using commercial Degussa P25 TiO_2 powders (P25) (Degussa AG, Dusseldorf, Germany). The films were annealed at 450 °C for 30 min and their thickness was about 15 μm. After calcination, the films were cooled to 80 °C for dye sensitization. The TiO2HS/CNT composite films were designated as CT-X (For P25/CNT films, designated as CP-X), where X (0, 0.05, 0.1, 0.2, 0.5 and 1) is related to the weight content of CNT to a 100 weight basis of the composite films (see Table 1).

Dye sensitization was performed by immersing TiO_2 films in 0.3 mM N719 ruthenium dye (Solaronix S.A., Lausanne, Switzerland) ethanol solution for at least 12 h at room temperature in a sealed beaker. The extent of sensitization was estimated by comparing the colors at the top and bottom of the film. The sensitization was completed after the colors at the top and the bottom were same. The sensitized films were washed once in anhydrous alcohol, and then dried in an oven at 80 °C for 2 h. A solar cell was assembled in a typical sandwich-type cell by placing a platinum-coated conducting glass on the dye-sensitized electrode separated by a ca. 50 μm polymer spacer. The assembled cell was then clipped together as an open cell. The active area of the cells was 4 mm × 4 mm. An electrolyte was prepared with 0.3 M LiI (Sigma–Aldrich Corp., St. Louis, MO, USA), 0.05 M I_2 (Sigma–Aldrich Corp., St. Louis, MO, USA), 0.6 M 1-propyl-3-methylimidazolium iodide (Suzhou Zhongsheng Chemical Co., Ltd., Suzhou, China), and 0.5 M *tert*-butylpyridine (Sigma–Aldrich Corp., St. Louis, MO, USA) in dry acetonitrile (Shanghai Chemical Reagent Factory of China, Shanghai, China). To ensure the same batch of electrolyte used for every sample, a large amount of electrolyte solution was prepared

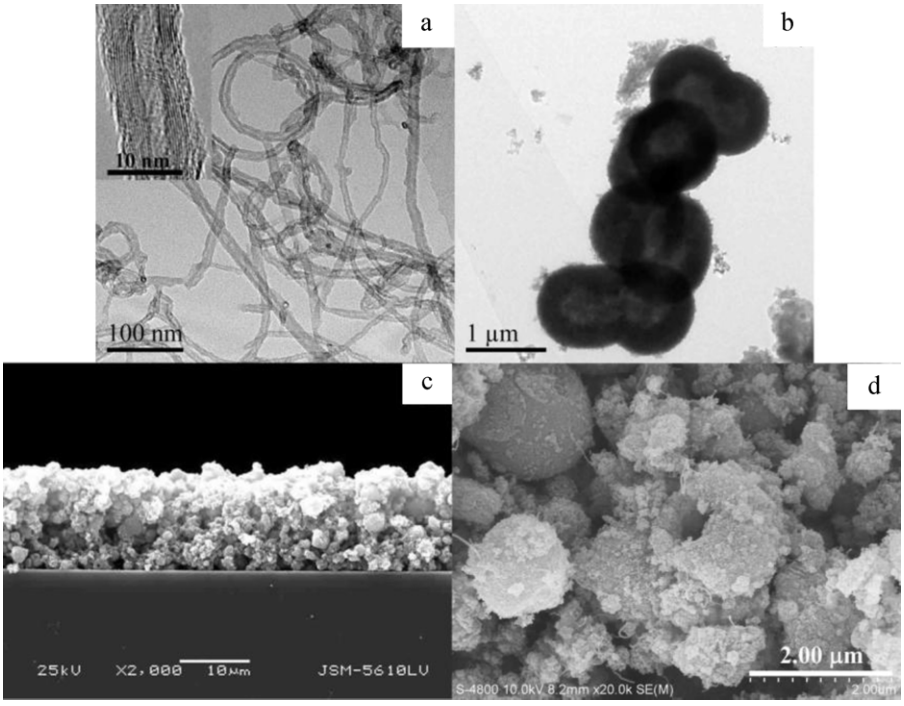

Fig. 1. TEM images of acid-treated CNT (a) and anatase TiO_2 hollow spheres (b), SEM images of cross-section (c) and surface (d) of the CT-0.5 composite film electrode. Inset in (a) showing HRTEM images of acid-treated CNT.

at first and then divided into several smaller glass vials. All vials were sealed and stored in a vacuum desiccator. The electrolyte was injected into the open cell from the edges and a thin layer of electrolyte was attracted into the inter-electrode space by capillary forces, and the cell was tested immediately.

2.3. Characterization and measurements

The morphology observation was performed by a JSM-5610LV scanning electron microscopy (SEM, JEOL Ltd., Tokyo, Japan) at an accelerating voltage of 25 kV and a S-4800 field emission SEM (FESEM, Hitachi Ltd., Tokyo, Japan), which is linked with an Oxford Instruments X-ray analysis system, at an accelerating voltage of 10 kV. X-ray diffraction (XRD) patterns were obtained on a D/MAX-RB X-ray diffractometer (Rigaku Corp., Tokyo, Japan) using Cu Kα irradiation at a scan rate (2θ) of $0.05^\circ\,s^{-1}$ and were used to determine the phase structures of the obtained samples. The accelerating voltage and applied current were 40 kV and 80 mA, respectively. The crystallite size of anatase titania was quantitatively calculated by Scherrer formula ($d = 0.9\lambda/B\cos\theta$, where d, λ, B and θ are crystallite size, Cu Kα wavelength (0.15418 nm), full width at half maximum intensity (FWHM) of (1 0 1) peak in radians and Bragg's diffraction angle, respectively) after correcting the instrumental broadening. Transmission electron microscopy (TEM) analyses were conducted by a JEM-2100F electron microscope (JEOL Ltd., Tokyo, Japan), using a 200 kV accelerating voltage. Nitrogen adsorption–desorption isotherms were obtained on an ASAP 2020 (Micromeritics Instruments Corp., Norcross, GA, USA) nitrogen adsorption apparatus. Photoluminescence (PL) spectra were measured at room temperature on a Fluorescence Spectrophotometer (F-7000, Hitachi Ltd., Tokyo, Japan) using a 315 nm excitation wavelength at a scan speed of 1200 nm min^{-1} with the PMT voltage of 700 V. Raman spectra were recorded at room temperature using a micro-Raman spectrometer (InVia, Renishaw PLC, Gloucestershire, UK) in the backscattering geometry with a 514.5 nm Ar^+ laser as an excitation source. UV–visible diffuse reflectance spectra (UV–vis DRS) of the as-prepared samples were obtained on a UV–visible spectrophotometer (UV-2550, Shimadzu Corp., Tokyo, Japan). $BaSO_4$ was used as a reflectance standard in a UV–visible diffuse reflectance experiment.

The electrochemical impedance spectroscopy (EIS) measurements were performed by a computer-controlled electrochemical work station with impedance analyzer (CHI660C Instruments, Shanghai Chenhua Instrument Corp., Shanghai, China) in a two-electrode configuration. The photoanode was used as a working electrode and the Pt electrode as a counter electrode. The measurements were carried out by applying bias of the open circuit voltage (V_{OC}) and recorded over a frequency range of 0.005–10^5 Hz with ac amplitude of 10 mV.

The photocurrent–voltage I–V characteristic curves and the transient photocurrent curves were measured using an electrochemical analyzer (CHI660C Instruments, Shanghai Chenhua Instrument Corp., Shanghai, China) controlled by a computer. The light was produced by a solar simulator (91160, Newport Corp., Irvine, CA, USA) at 100 mW cm^{-2} (1 sun) intensity. The active area of DSSCs was 4 mm × 4 mm. The photoelectric conversion efficiency (η) was calculated according to the following equation:

$$\eta\,(\%) = \frac{V_{OC} I_{SC} FF}{P_{in}} \times 100 \tag{1}$$

The incident monochromatic photoelectric conversion efficiency (IPCE) was measured using Newport's QE/IPCE Measurement Kit, where a monochromator (Cornerstone 130 1/8 m, Newport Corp., Irvine, CA, USA) was used to obtain the monochromatic light from a 300 W Xe lamp (Newport, model no. 6258). The IPCE scan is taken based on an AC (8 Hz) measurement. The IPCE was defined as following equation:

$$\mathrm{IPCE}\,(\%) = \frac{12,400 \times I_{SC}(\mu\mathrm{A\ cm^{-2}})}{\lambda(\mathrm{nm}) \times P_{in}(\mu\mathrm{W\ cm^{-2}})} \tag{2}$$

In the above two formulas, η is the global efficiency, V_{OC}, I_{SC}, and FF are open circuit voltage, short circuit current density, and fill factor, respectively. P_{in} and λ are the light energy and wavelength of the incident monochromatic light, respectively. The measurements

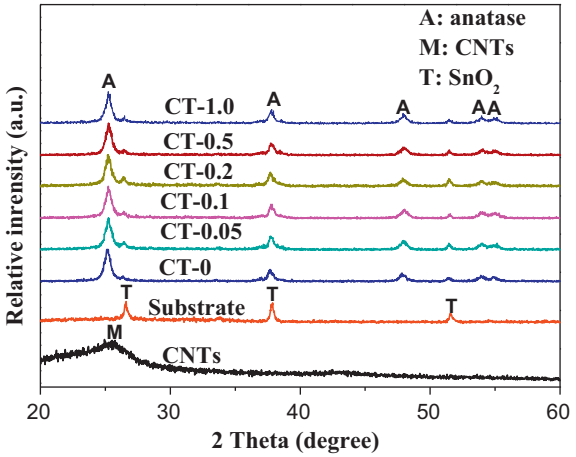

Fig. 2. XRD patterns of acid-treated CNT, FTO glass substrate and the CT-0, CT-0.05, CT-0.1, CT-0.2, CT-0.5 and CT-1.0 composite film electrodes.

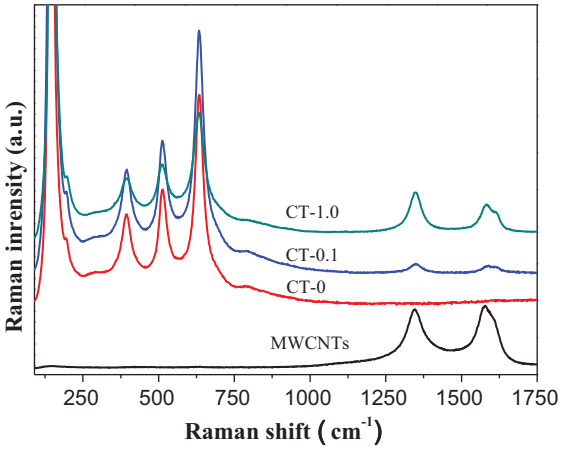

Fig. 3. Comparison of the Raman spectra of acid treated CNT and the CT-0, CT-0.1 and CT-1.0 composite film electrodes.

were repeated three times for each sample, and the experimental error was found to be within ca. 5%.

3. Results and discussion

3.1. Morphology and crystal structures

Acid-treated CNT and anatase TiO_2 hollow spheres were used to fabricate the TiO2HS/CNT composite film electrodes in this study. The TEM images of acid-treated CNT and TiO_2 hollow spheres, and the cross-section and surface SEM images of the CT-0.5 composite film electrode are shown in Fig. 1. The CNT possess a nanoscale tubular morphology with diameters of ca. 10–12 nm (Fig. 1a) and a multi-walled structure (inset in Fig. 1a). TEM image of the TiO_2 hollow spheres indicates that the sizes of the prepared hollow spheres are in the range of 500–1000 nm, and nearly all the spheres consist of a 300–700 nm hollow cavity (Fig. 1b). It can be seen from Fig. 1c that the TiO2HS/CNT composite films appear porous structures and the film thickness is about 15 μm. Fig. 1d shows that the CNT were well-dispersed on the surface of the TiO_2 spheres, and there was good contact between the CNT and TiO_2 spheres. Further observation indicates that the composite film appears a disordered macroporous network, besides the void spaces between nanoparticles, there are many large void spaces of several tens to several hundreds nm in size within TiO_2 films.

The phase structure, crystallite size, and crystallinity of TiO_2 are of great influence on the photoelectric conversion efficiency (η) of DSSCs [29,35]. XRD was used to characterize the difference of phase structures and crystallite sizes of the samples. Fig. 2 shows XRD patterns of acid-treated CNT, FTO glass substrate, and TiO2HS/CNT composite films. For pure FTO glass substrate, three strong and sharp diffraction peaks (at $2\theta = 26.6^\circ$, 37.8° and 51.8°) are observed and these peaks are attributed to SnO_2 (space group: $P4_2/mnm$ (136); $a = 4.750$ Å, $c = 3.198$ Å, JCPDS No. 46-1088) [29,36]. As for TiO2HS/CNT composite films, the peaks at 25.3°, 37.8°, 48.1°, 54.0° and 55.1° are clearly observed, indicating the existence of anatase phase [JCPDS No. 21-1272, space group: $I4_1/amd$ (141); $a = 3.785$ Å, $c = 9.514$ Å]. However, no apparent peaks from CNT are observed due to their low concentration. Another cause is that its most intense diffraction peak (0 0 2) is largely overlapped with anatase (1 0 1) peak. The existence of CNT can be determined by the following Raman spectra. Further observation indicates that the full width at half maximum (FWHM) of the anatase peaks for TiO2HS/CNT composite films are slightly broadened with increasing amount of CNT. Such a FWHM broadening implies a decrease in the anatase crystallite size. In the present case, considering possible interference from the CNT over anatase (1 0 1) peak, anatase TiO_2 (2 0 0) reflection plane ($2\theta = 48.1^\circ$) was selected to estimate crystallite sizes based on FWHM broadening using Scherrer formula. As shown in Table 1, the average crystallite size for pure TiO_2 is ca. 15.7 nm, while that for the TiO2HS/CNT nanocomposites slightly decrease from 15.7 to 13.9 with increasing CNT loading from 0.05 to 1 wt%. This result suggests that the presence of the CNT in the CT-X composite films hinders the crystallite growth of anatase. Moreover, the crystallinity of TiO_2 in the TiO2HS/CNT composite films is lowered due to CNT loading, especially with higher content (see Table 1).

3.2. Raman spectra

To determine the presence of CNT in the CT-X composite film electrodes after 450 °C calcination, Raman spectroscopy was applied to characterize the microstructures of TiO2HS/CNT composite film electrodes. Fig. 3 shows the comparison of the Raman spectra of acid treated CNT, pure TiO_2 (CT-0) and TiO2HS/CNT composite film electrodes (CT-0.1 and CT-1.0). For pure TiO_2 (CT-0) sample, four strong peaks at 150, 395.1, 512.5 and 636.7 cm^{-1} are clearly observed, which respectively correspond to the $E_{g(1)}$, $B_{1g(1)}$, $A_{1g} + B_{1g(2)}$ and $E_{g(2)}$ modes of anatase TiO_2 [37,38]. For acid-treated CNT, two typical Raman feature peaks are observed at approximately 1345 and 1580 cm^{-1}, which is assigned to the characteristic D-band at 1345 cm^{-1} and G-band at 1580 cm^{-1} of CNT, corresponding to the disordered mode and tangential mode, respectively [31,39,40]. In the case of TiO2HS/CNT composite film electrodes (CT-0.1 and CT-1.0), all the Raman bands for anatase and CNT are still observed except the anatase Raman bands for TiO2HS/CNT composite films are slightly broadened and become weak comparing with the pure TiO_2 film (CT-0). The broadening of peaks and the decrease of the intensities also imply the decease of the average crystallite size and crystallinity of anatase (Table 1). Importantly, the two obvious peaks corresponding to CNT are observed in the Raman spectra of the composite film electrodes (CT-0.1 and CT-1.0). Also, with increasing the CNT loading, the peak intensity increases. Further observation indicates that the peaks assigned to CNT within the composite films exhibit a slight blue-shift relative to acid-treated CNT, indicating the interfacial interaction between TiO_2 and acid-treated CNT due to the 450 °C calcination [7]. The blue-shift is also from the strain effects at the TiO2HS/CNT interfaces, which may influence the vibrational frequencies [19,41].

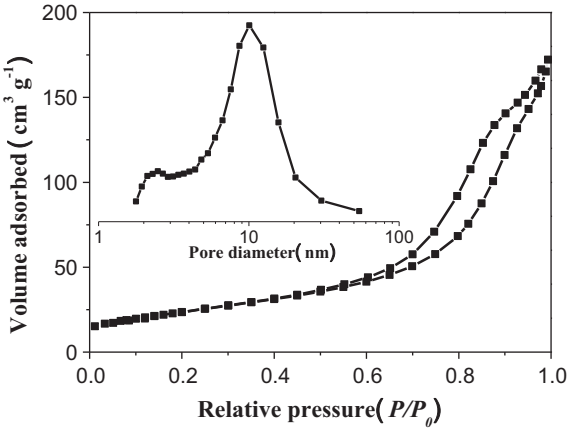

Fig. 4. Nitrogen adsorption–desorption isotherms and the corresponding pore-size distribution curves (inset) of TiO2HS/CNT composite powders scraped from the CT-0.1 composite film electrodes.

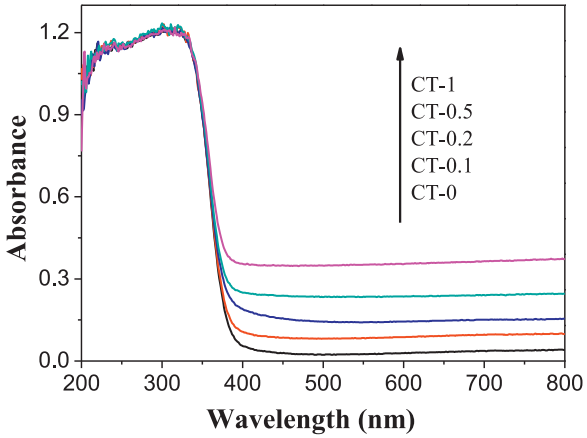

Fig. 5. UV–vis diffuse reflectance spectra of the CT-0, CT-0.1, CT-0.2, CT-0.5 and CT-1.0 composite film electrodes.

3.3. BET surface areas and pore structure

Fig. 4 shows nitrogen adsorption–desorption isotherms and the corresponding pore-size distribution curves (inset) of the TiO2HS/CNT composite powders scraped from the CT-0.1 composite film electrode. The sample shows type IV isotherms with H2-type hysteresis loops according to Brunauer–Deming–Deming–Teller (BDDT) classification [42], indicating the presence of mesopores (2–50 nm). The sample shows bimodal mesopore size distributions (inset in Fig. 4), that is, smaller mesopores with peak pore diameters of ca. 2.5 nm and bigger mesopores with peak pore diameters about 10.1 nm. This bimodal pore-size distribution is ascribed to two different pores: finer intra-aggregated pore within the agglomerated particles and large inter-aggregated pore produced by inter-aggregated secondary particles [43–45]. The physicochemical properties of TiO2HS/CNT composite powders scraped from the composite film electrodes are shown in Table 1. All the samples have mesoporous structures. With increasing CNT content, the S_{BET} and the pore volume of the TiO2HS/CNT composites increase slightly. This is due to the fact that the CNT have a larger surface area (244 m^2/g) and a lower density (0.8–1.2 cm^3/g) than pure TiO_2 sample (CT-0). Since macroporous information of the film electrodes cannot be directly obtained by N_2 adsorption–desorption analyses, the macroporous structures are clearly observed by the previous SEM and TEM images (Fig. 1), indicating that the 450 °C-calcined composite film contains 3-dimensional continuous macroporous/mesoporous network from several, several tens, several hundred nm sized pores. The prepared hierarchically porous structures not only enhance the absorption of light, but also provide efficient transport pathways to electrolyte molecules.

3.4. UV–vis spectra

Fig. 5 shows comparison of UV–vis diffuse reflection spectra of the TiO2HS/CNT composite film electrodes (CT-X, X = 0.1, 0.2, 0.5 and 1) and pure TiO_2 film (CT-0). A significant increase in the absorption at wavelengths shorter than 400 nm is assigned to the intrinsic band gap absorption of TiO_2 [46]. A comparison of the UV–vis spectra of all TiO2HS/CNT composite films with that of pure TiO_2 (CT-0) shows an enhanced absorption in the visible-light region; this visible absorption increases with increasing the CNT loading. There is no visible change in the absorption edges of the TiO2HS/CNT composite film electrodes (CT-X, X = 0.1, 0.2, 0.5 and 1) in comparison to pure TiO_2 (CT-0 sample), implying that CNT was not incorporated into the lattice of TiO_2 but it only contacted with its surface. This is easy to be understood because CNT is stable at 450 °C and is not decomposed. The enhancement of visible light absorption means the increase in the light-harvesting capability of the electrodes [3,29].

3.5. Transient photocurrent measurement

The previous studies have indicated that the recombination rate of photogenerated electrons and holes is an important factor influencing the photoelectron conversion efficiency of DSSCs [5,47,48]. Consequently, reducing the e^-/h^+ recombination rate and enhancing the electron transport and their lifetime become effective methods toward improving the performance of the DSSCs. Because CNT has novel morphology and good electrical conductivity, the TiO2HS/CNT composite films are thought to enhance the transport of the electrons within TiO_2 films and their photoelectric conversion efficiencies. Thus, the PL spectra were used to determine the efficiency of the charge recombination, as shown in Fig. 6. The pure TiO_2 film shows a broad PL emission band, which was similar to our previous reported results [49,50]. The peak intensity of the PL spectra of the composite samples is lower than that of pure TiO_2, and decreases with increasing CNT loading. This indicates that incorporation of CNT within TiO_2 films can reduce the e^-/h^+ recombination rate [49–51]. Low PL intensity for the composite films also implies that the photoinduced electrons resulting from the excited

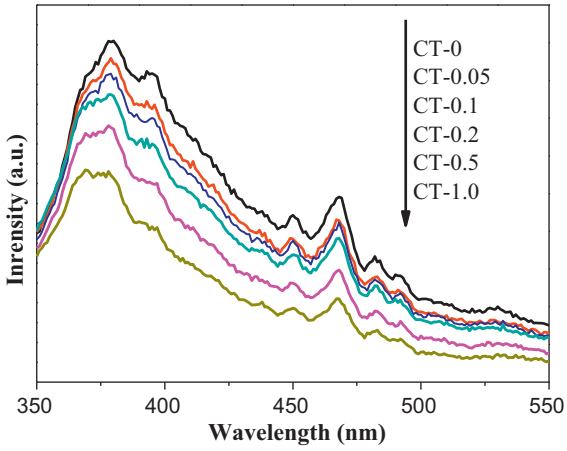

Fig. 6. PL spectra of the CT-0, CT-0.05, CT-0.1, CT-0.2, CT-0.5 and CT-1.0 composite film electrodes.

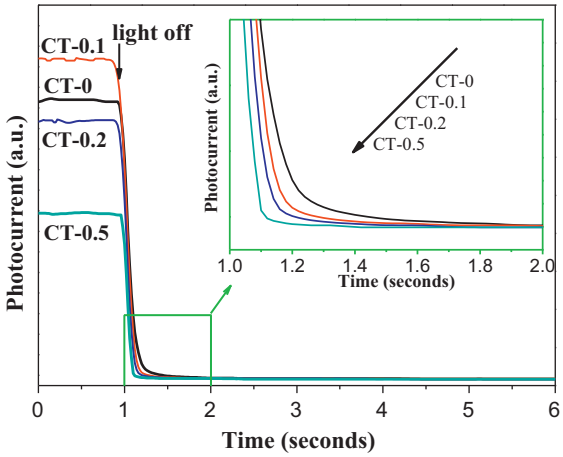

Fig. 7. Transient photocurrent and high-magnification curves (inset) of DSSCs based on the CT-0, CT-0.1, CT-0.2 and CT-0.5 composite film electrodes.

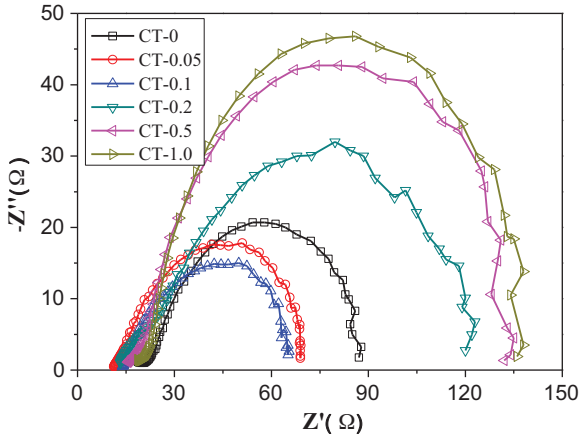

Fig. 9. Nyquist plots of DSSCs based on the CT-0, CT-0.05, CT-0.1, CT-0.2, CT-0.5 and CT-1.0 composite film electrodes.

dye can effectively inject the conduction band of TiO_2, and, then be collected by CNT, decreasing the charge recombination (electrons and oxidized dye (D^+)) within the DSSCs. Furthermore, CNT possess a light-harvesting property (like dyes) (see Fig. 5). This also results in the low PL peak intensity of the composite films. Hence, in order to further understand the effects of CNT on the charge recombination of DSSCs, the transient photocurrent of DSSCs with various composite anodes was investigated. Fig. 7 shows the rise and fall of the I_{SC} during one on–off cycle of illumination at 100 mW cm^{-2}. The time required for the fall of the I_{SC} by 90% in the case of the DSSCs with composite is faster than that with pristine TiO_2 film. Also, the required time decreases with increasing the amount of CNT. This indicates that the photogenerated electrons from dyes are more easily trapped by the surface electron trap of pure TiO_2 electrode than that of the composite films, resulting in a slower photocurrent response [52–54]. Generally, the transportation of photogenerated electrons in the DSSCs is strongly influenced by (1) trapping and (2) detrapping of the photoinduced electrons in the TiO_2 film electrodes. Electronic trapping is much more rapid than electronic detrapping (by ~3 orders of magnitude), thus resulting in almost all photoinjected electrons located in trap states [52,55]. Furthermore, the charge recombination are mainly from the recapture of injected electrons in these traps by the oxidized dye (D^+) anchored on the TiO_2 surface (3) or back reaction with the oxidized component of the electrolyte, I_3^- (4) [56,57]. Hence, supposing electronic detrapping can be enhanced and the charge recombination of DSSCs is expected to be inhibited by incorporating CNT into the TiO_2 films due to its good electrical conductivity. Based on the above PL and transient photocurrent experiments, we confirm that introducing CNT into TiO_2 electrodes can reduce the recombination of charge carriers and enhance the performance of DSSCs.

3.6. IPCE and impedance analysis

Fig. 8 displays the comparison of IPCE curves of the DSSCs made from the CT-0, CT-0.1 and CT-0.2 film electrodes, in which IPCE were normalized to a common value of 1 at their maximum (530 nm). As can be seen, the CT-0.1 solar cell shows much higher IPCE values than that of the CT-0 solar cell, implying that the incorporation of a small amount of CNT into TiO_2 films enhance the photoelectric conversion efficiency of the DSSCs. However, the IPCE values decreases at a higher CNT content (0.2 wt%). This is due to the fact that CNT can absorb visible light at the wavelengths above 400 nm, they display light-harvesting competition with the dye molecules, and thus reduce the photovoltaic conversion performance for the TiO2HS/CNT DSSCs [5].

Electrochemical impedance spectroscopy (EIS) has been widely used to investigate electronic and ionic reaction in dye-sensitized solar cells (DSSCs). A theoretical model has been proposed to interpret the frequency response of the device. The high-frequency response is due to the charge transfer (or electrochemical reaction) at the Pt counter electrode, while the intermediate-frequency response is associated with the electron transport and transfer at TiO_2/dye/electrode interface. The low-frequency region reflects the

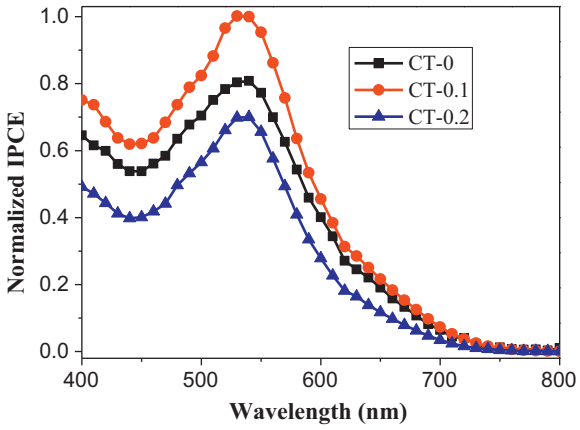

Fig. 8. Normalized IPCE of DSSCs based on the CT-0, CT-0.1 and CT-0.2 composite film electrodes.

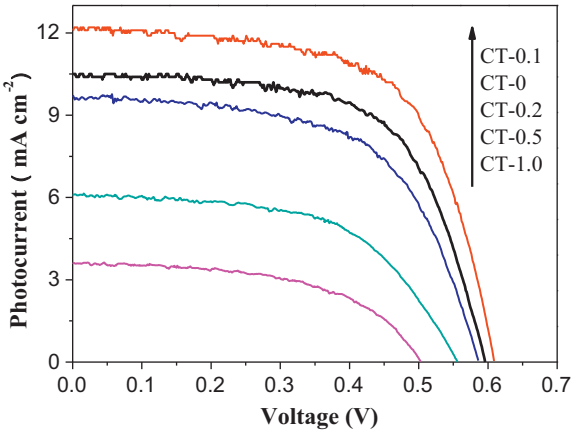

Fig. 10. Comparison of the *I–V* characteristics of DSSCs based on the CT-0, CT-0.1, CT-0.2, CT-0.5 and CT-1.0 composite film electrodes.

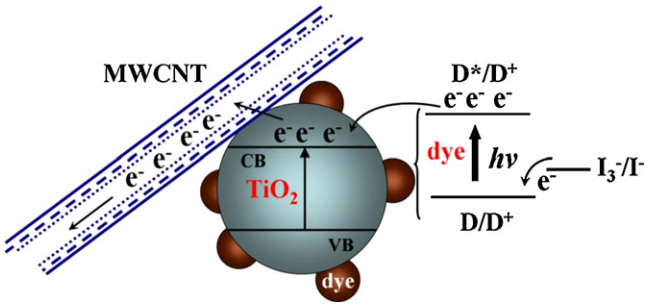

Fig. 11. Proposed mechanism for the enhanced electron transfer in the TiO2HS/CNT composite film electrodes.

Warburg diffusion process of I^-/I_3^- in the electrolyte [58]. The EIS Nynquist plots of the DSSCs based on the TiO2HS/CNT composite films are shown in Fig. 9. The semicircle in the middle-frequency region is assigned to charge transfer at the TiO_2/dye/electrode interface [59,60]. Compared with that of the CT-0 solar cell, the value of the charge transport resistance at the TiO_2/dye/electrolyte interface of CT-0.05 DSSC slightly decreases. It is due to the 1D CNT in favor of the photogenerated charges transfer, thus lowering the charge recombination [61]. The CT-0.1 DSSC has the smallest interfacial resistance, which indicates a fastest interfacial electron transfer and high energy conversion efficiency. However, with further increases in the CNT loading (from 0.2 to 1.0 wt%), the interfacial resistance increased. This is due to the fact that higher CNT loading causes light-harvesting competition between the dye-sensitizer and CNT [5], resulting in fewer electrons injected from the dye to the TiO2HS/CNT composite electrodes.

3.7. Photocurrent–voltage characteristics

Comparison of the *I–V* characteristics of the DSSCs based on TiO2HS/CNT and P25/CNT composite film electrodes is shown in Fig. 10 and Table 2. The photoelectric conversion performances of the DSSCs based on the TiO2HS/CNT composite film electrodes are strongly dependent on the CNT loading in the electrodes. The value of V_{OC} increases from 0.596 to 0.609 V with the increase in CNT content from 0 to 0.1 wt%. This is due to the fact that the incorporation of a small amount of CNT into the TiO_2 films can reduce the charge recombination rate and resistance [61]. Therefore, it is not surprising that the values of V_{OC} and I_{SC} of a DSSC increase in the presence of a small amount of CNT. The enhanced I_{SC} (from 10.5 to 12.1 mA cm^{-2}) is ascribed to the enhancement of the collection and transport of electrons [19,59]. Under optimal conditions, the efficiency of the CT-0.1 solar cell is 4.71%. The improvement in energy conversion efficiency is due to the decrease in the charge transport resistance at the TiO_2/dye/electrolyte interface, the decreased charge recombination of excited electrons and holes, and the efficient electron transport by CNT, which enhance the transport of electrons from the films to FTO substrates (see Fig. 11). However, at higher CNT contents, the conversion efficiencies decrease. A higher CNT loading causes CNT agglomeration and light-harvesting competition between the dye and CNT, and consequently increases the charge transport resistance at the TiO_2/dye/electrolyte interface and reduces the efficiency. Further experiments show that the η (4.71%) of the CT-0.1 DSSC is higher than that (3.78% for CP-0, 4.11% for CP-0.1 and 4.52% for CP-0.2) of P25/CNT composite DSSC with the same thickness. P25 is well known to have a superior photocatalytic activity and photoelectric conversion efficiency. The enhanced performance of TiO2HS/CNT cells is due to their high specific surface areas and hierarchically nanoporous structures. The higher specific surface areas enhance adsorption of dye molecules and the light harvesting, the hollow spheres are also expected to enhance the diffusion of electrolyte in the cell because the pore volume of hollow spheres is higher than that of P25 particle films. It is well known that the efficient diffusion of I_3^-/I^- to regenerate the dye is important to the photovoltaic response of the solar cells.

Table 2
Comparison of the *I–V* characteristics of DSSCs based on TiO2HS/CNT and P25/CNT composite films.

Samples	I_{SC} (mA cm^{-2})	V_{OC} (V)	FF	η (%)
CT-0	10.5	0.596	0.630	3.94
CT-0.05	11.1	0.605	0.634	4.26
CT-0.1	12.1	0.609	0.639	4.71
CT-0.2	9.72	0.586	0.593	3.38
CT-0.5	6.11	0.556	0.568	1.93
CT-1	3.63	0.503	0.537	0.98
CP-0	9.98	0.589	0.643	3.78
CP-0.05	10.3	0.613	0.618	3.90
CP-0.1	11.0	0.605	0.618	4.11
CP-0.2	11.7	0.607	0.636	4.52
CP-0.5	9.78	0.587	0.535	3.07
CP-1	7.21	0.526	0.382	1.45

4. Conclusions

Dye-sensitized solar cells (DSSCs) based on anatase TiO_2 hollow spheres/multi-walled carbon nanotube nanocomposite films are fabricated by a direct mechanical mixing and doctor blade method. The CNT loading clearly influences the textural properties (including crystallite size, specific surface areas, porosity and pore volume) and photoelectric conversion efficiency of the TiO2HS/CNT nanocomposite film electrodes. As a result, the TiO2HS/CNT nanocomposite films with low loadings (<0.1 wt%) show enhanced photoelectric conversion efficiency, as compared with pristine TiO_2 counterparts. On the other hand, high CNT loadings (>0.1 wt%) result in the decrease in the efficiency. Under optimal conditions, the efficiency of the CT-0.1 solar cell is 4.71%, which is higher than that (3.94%) of pure TiO_2 cells. The improvement in the conversion efficiency is due to the fact that CNT reduce the electrolyte/electrode interfacial resistance, the recombination rate of excited electrons and holes, and enhance the transport of electrons from the films to FTO substrates. The decrease of the conversion efficiency at high CNT loadings (>0.1 wt%) is due to light-harvesting competition between CNT and dye molecules, which influences the light adsorption of the dye-sensitizer, and consequently reduces the efficiency. The performances of TiO2HS/CNT cells are also compared with P25/CNT composite cells at the same film thickness and their optimal efficiencies under the experimental conditions are 4.71% and 4.52%, respectively. The enhanced performance of TiO2HS/CNT cells is due to their higher surface area and hierarchically nanoporous structures. This study will provide new insight into fabrication and structural design of highly efficient dye-sensitized solar cells.

Acknowledgements

This work was partially supported by the National Natural Science Foundation of China (20877061 and 51072154) and the Natural Science Foundation of Hubei Province (2010CDA078). Also, this work was financially supported by the National Basic Research Program of China (2007CB613302 and 2009CB939704).

References

[1] B. O'Regan, M. Gratzel, Nature 353 (1991) 737.
[2] J.G. Yu, J.J. Fan, K.L. Lv, Nanoscale 2 (2010) 2144.
[3] B. Tan, Y.Y. Wu, J. Phys. Chem. B 110 (2006) 15932.
[4] M.K. Nazeeruddin, A. Kay, I. Rodicio, R. Humphry-Baker, E. Muller, P. Liska, N. Vlachopoulos, M. Gratzel, J. Am. Chem. Soc. 115 (1993) 6382.

[5] I. Mora-Sero, S. Gimenez, F. Fabregat-Santiago, R. Gomez, Q. Shen, T. Toyoda, J. Bisquert, Acc. Chem. Res. 42 (2009) 1848.
[6] M. Gratzel, Inorg. Chem. 44 (2005) 6841.
[7] G.J. Meyer, Inorg. Chem. 44 (2005) 6852.
[8] J.L. Li, L.D. Wang, X.M. Kong, B.B. Ma, Y.T. Shi, C. Zhan, Y. Qiu, Langmuir 25 (2009) 11162.
[9] L. Zhao, J.G. Yu, J.J. Fan, P.C. Zhai, S.M. Wang, Electrochem. Commun. 11 (2009) 2052.
[10] B. Liu, E.S. Aydil, J. Am. Chem. Soc. 131 (2009) 3985.
[11] M. Adachi, Y. Murata, J. Takao, J.T. Jiu, M. Sakamoto, F.M. Wang, J. Am. Chem. Soc. 126 (2004) 14943.
[12] S. Iijima, Nature 354 (1991) 56.
[13] A. Kongkanand, P.V. Kamat, ACS Nano 1 (2007) 13.
[14] H.T. Yu, X. Quan, S. Chen, H.M. Zhao, J. Phys. Chem. C 111 (2007) 12987.
[15] Y. Yu, J.C. Yu, J.G. Yu, Y.C. Kwok, Y.K. Che, J.C. Zhao, L. Ding, W.K. Ge, P.K. Wong, Appl. Catal. A 289 (2005) 186.
[16] S. Muduli, W. Lee, V. Dhas, S. Mujawar, M. Dubey, K. Vijayamohanan, S.H. Han, S. Ogale, ACS Appl. Mater. Interface 1 (2009) 2030.
[17] T.Y. Lee, P.S. Alegaonkar, J.B. Yoo, Thin Solid Films 515 (2007) 5131.
[18] C.Y. Yen, Y.F. Lin, S.H. Liao, C.C. Weng, C.C. Huang, Y.H. Hsiao, C.C.M. Ma, M.C. Chang, H. Shao, M.C. Tsai, C.K. Hsieh, C.H. Tsai, F.B. Weng, Nanotechnology 19 (2008) 375305.
[19] S.L. Kim, S.R. Jang, R. Vittal, J. Lee, K.J. Kim, J. Appl. Electrochem. 36 (2006) 1433.
[20] T. Sawatsuk, A. Chindaduang, C. Sae-kung, S. Pratontep, G. Tumcharern, Diamond Relat. Mater. 18 (2009) 524.
[21] S.W. Liu, J.G. Yu, M. Jaroniec, J. Am. Chem. Soc. 132 (2010) 11914.
[22] J.G. Yu, Y.R. Su, B. Cheng, Adv. Funct. Mater. 17 (2007) 1984.
[23] J.G. Yu, Q.J. Xiang, M.H. Zhou, Appl. Catal. B 90 (2009) 595.
[24] C. Trapalis, N. Todorova, M. Anastasescu, C. Anastasescu, M. Stoica, M. Gartner, M. Zaharescu, T. Stoica, Thin Solid Films 517 (2009) 6243.
[25] J.G. Yu, J. Zhang, Dalton Trans. 39 (2010) 5860.
[26] J.G. Yu, L. Shi, J. Mol. Catal. A 326 (2010) 8.
[27] A. Syoufian, K. Nakashima, J. Colloid Interface Sci. 313 (2007) 213.
[28] S.W. Liu, J.G. Yu, S. Mann, Nanotechnology 20 (2009) 356802.
[29] J.G. Yu, J.J. Fan, L. Zhao, Electrochim. Acta 55 (2010) 597.
[30] G.S. Kim, H.K. Seo, V.P. Godble, Y.S. Kim, O.B. Yang, H.S. Shin, Electrochem. Commun. 8 (2006) 961.
[31] W. Zhou, K. Pan, L.L. Zhang, C.G. Tian, H.G. Fu, Phys. Chem. Chem. Phys. 11 (2009) 1713.
[32] R.Q. Yu, L.W. Chen, Q.P. Liu, J.Y. Lin, K.L. Tan, S.C. Ng, H.S.O. Chan, G.Q. Xu, T.S.A. Hor, Chem. Mater. 10 (1998) 718.
[33] X.B. Yan, B.K. Tay, Y. Yang, J. Phys. Chem. B 110 (2006) 25844.
[34] X.H. Li, J.L. Niu, J. Zhang, H.L. Li, Z.F. Liu, J. Phys. Chem. B 107 (2003) 2453.
[35] N.G. Park, J.V.D. Lagemeaat, A.J. Frank, J. Phys. Chem. B 104 (2000) 8989.
[36] J.G. Yu, M.H. Zhou, Nanotechnology 19 (2008) 045606.
[37] S.W. Liu, J.G. Yu, S. Mann, J. Phys. Chem. C 113 (2009) 10712.
[38] G.J. Hu, X.F. Meng, X.Y. Feng, Y.F. Ding, S.M. Zhang, M.S. Yang, J. Mater. Sci. 42 (2007) 7162.
[39] U.J. Kim, C.A. Furtado, X.M. Liu, G.G. Chen, P.C. Eklund, J. Am. Chem. Soc. 127 (2005) 15437.
[40] S. Osswald, E. Flahaut, Y. Gogotsi, Chem. Mater. 18 (2006) 1525.
[41] C.Y. Xu, P.X. Zhang, L. Yan, J. Raman Spectrosc. 32 (2001) 862.
[42] K.S.W. Sing, D.H. Everett, R.A.W. Haul, L. Moscou, R.A. Pierotti, J. Rouquerol, T. Siemieniewska, Pure Appl. Chem. 57 (1985) 603.
[43] J.G. Yu, J.C. Yu, M.K.P. Leung, W.K. Ho, B. Cheng, X.J. Zhao, J.C. Zhao, J. Catal. 217 (2003) 69.
[44] J.G. Yu, G.H. Wang, B. Cheng, M.H. Zhou, Appl. Catal. B 69 (2007) 171.
[45] J.G. Yu, L.J. Zhang, B. Cheng, Y.R. Su, J. Phys. Chem. C 111 (2007) 10582.
[46] Q.J. Xiang, J.G. Yu, B. Cheng, H.C. Ong, Chem. Asian J. 5 (2010) 1466.
[47] M. Gratzel, J. Photochem. Photobiol. A 164 (2004) 3.
[48] T.A. Heimer, E.J. Heilweil, C.A. Bignozzi, G.J. Meyer, J. Phys. Chem. A 104 (2000) 4256.
[49] Q.J. Xiang, K.L. Lv, J.G. Yu, Appl. Catal. B 96 (2010) 557.
[50] J.G. Yu, L.F. Qi, M. Jaroniec, J. Phys. Chem. C 114 (2010) 13118.
[51] X.Z. Li, F.B. Li, C.L. Yang, W.K. Ge, J. Photochem. Photobiol. A 141 (2001) 209.
[52] A.C. Fischer, L.M. Peter, E.A. Ponomarev, A.B. Walker, K.G.U. Wijayantha, J. Phys. Chem. B 104 (2000) 949.
[53] K. Schwartsburg, F. Wllig, Appl. Phys. Lett. 58 (1991) 2520.
[54] X.M. Qian, D.Q. Qin, Q. Song, Y.B. Bai, T.J. Li, X.Y. Tang, E.K. Wang, S.J. Dong, Thin Solid Films 385 (2001) 152.
[55] I.A. Shkrob, M.C. Sauer, J. Phys. Chem. B 108 (2004) 12497.
[56] Z.P. Zhang, S.M. Zakeeruddin, B.C. O'Regan, R. Humphry-Baker, M. Gratzel, J. Phys. Chem. B 109 (2005) 21818.
[57] A. Hagfeldt, M. Gratzel, Chem. Rev. 95 (1995) 49.
[58] Q. Wang, J.E. Moser, M. Gratzel, J. Phys. Chem. B 109 (2005) 14945.
[59] K.M. Lee, C.W. Hu, H.W. Chen, K.C. Ho, Sol. Energy Mater. Sol. Cells 92 (2008) 1628.
[60] S. Yanagida, Y.H. Yu, K. Manseki, Acc. Chem. Res. 42 (2009) 1827.
[61] J.G. Yu, T.T. Ma, S.W. Liu, Phys. Chem. Chem. Phys. 13 (2011) 3491.